Melting of tantalum at multi-megabar pressures on the nanosecond timescale

R. G. Kraus, F. Coppari, D. E. Fratanduono, R. F. Smith, A. Lazicki, C, Wehrenberg, and J. H. Eggert

Physics Division, Lawrence Livermore National Laboratory, Livermore, CA 94550

G. W. Collins

Mechanical Engineering Department,

University of Rochester, Rochester, NY 14627

(Dated: February 4, 2021)

Abstract

Tantalum was once thought to be the canonical BCC metal, but is now believed to transition to the PNMA phase at the high pressures and temperatures expected along the principal Hugoniot. Furthermore, there remains a significant discrepancy between static diamond anvil cell experiments and gas gun experiments in the measured melt temperatures at high pressures. Our in situ x-ray diffraction experiments on shock compressed tantalum show that it does not transition to the Pnma phase or other candidate phases at high pressure. We observe incipient melting at approximately 254±15 GPa and complete melting by 317±10 GPa. These incipient and complete melting transition pressures from the nanosecond timescale experiments presented here are consistent with what can be inferred from microsecond timescale gas gun sound velocity measurements. Furthermore, the observation of a coexistence region on the Hugoniot implies the lack of significant kinetics. Consequently, we find that kinetics of phase transitions cannot be used to explain the discrepancy between static and dynamic measurements of the tantalum melt curve. Using available high pressure thermodynamic data for tantalum and our measurements of the incipient and complete melting transition pressures, we are able to infer a melting temperature 8069^{+1250}_{-750} K at 254±15 GPa, which is consistent with ambient and recent static high pressure melt curve measurements.

Usage: Secondary publications and information retrieval purposes.

PACS numbers: May be entered using the `\pacs{#1}` command.

Structure: You may use the `description` environment to structure your abstract; use the optional argument of the `\item` command to give the category of each item.

I. INTRODUCTION

The melt curve represents the largest rheological transition a material can undergo, from a material with strength to one without. The melt curve at high pressure is also an extremely sensitive test of our understanding of material behavior as the free energy surfaces of the high-temperature solid and liquid are nearly parallel. Unfortunately, for some materials there remains significant discrepancy in our experimental measurements of the high-pressure melt curve. Tantalum in particular still remains an enigma, where shock compression techniques and a single static high-pressure study find agreement along a high-temperature melt curve [1–3] while numerous other static high pressure experiments continue to measure a relatively low melting temperature [4–6].

Due to the tremendous experimental efforts on both sides of the argument, one must focus on performing robust experiments utilizing techniques that are least prone to systematic error. There is general agreement that robust detection of liquid is the predominent issue with melt curve measurements. While rapid recrystallization, sound speed changes, latent heat signatures, and reflectivity features have been used to detect melting, most widely accepted is the detection of diffuse liquid scattering within in situ x-ray diffraction experiments. However, detection of liquid with x-ray diffraction often requires long recording times at elevated temperatures, which can lead to chemical reactions that systematically lower the inferred melt temperature. Consequently, the optimal experiment would heat the sample faster than ionic diffusivity in the sample and then utilize in situ x-ray diffraction to detect liquid scattering. Given that the ionic diffusivity in the liquid is of order of $5\text{x}10^{-9}$ m^2 s^{-1} [7], the heating timescale for few micron samples must be faster than a few hundred microseconds in order to ensure the sample is not permeated by material adjacent to the sample.

However, timescales this short lead to a second potential problem, which is the time dependent approach to the equilibrium phase, or the kinetics of phase transitions, causing the transition to occur at pressures or temperatures beyond those in equilibrium. Work by [8–10] and others suggest that shock wave measurements of melting, occcuring on the microsecond timescale, need to be significantly corrected to lower temperatures to account for the degree of superheating expected. However, Luo et al. [11, 12] analyzed the systematics of superheating signatures and concluded that superheating could not be sufficient to explain

the discrepancy in experimental measurements in tantalum and other refractory metals, as was also found in the study by [13].

In this work, we experimentally constrain the melt curve of tantalum at high pressure and high temperature using a fast x-ray diffraction measurement to ensure there is no time for chemical reactions. With in-situ x-ray diffraction, we are able to directly observe the shock melting transition on the nanosecond timescale, from a solid, to a mixed phase, to a pure liquid. To confirm that superheating is not significant, we compare these nanosecond dynamic compression experiments to previous microsecond dynamic compression experiments. We then use available thermodynamic data and our constraint on the shock melting transition pressures to infer the temperature on the high pressure melt curve of tantalum.

II. EXPERIMENTAL METHODS

Nanosecond duration laser driven shock compression experiments were performed at the Laboratory for Laser Energetics at the University of Rochester on the Omega laser facility. Using a single beam of the Omega laser focused with a random phase plate to a sixth order supergaussian spot size of 800 microns diameter and using energies from 57 to 126 J, single steady shock waves were driven into the 38 micron thick Kapton Type HN ablator, which then transmitted the shock into the high purity, Goodfellows 99.9%, 8 micron thick tantalum foil samples. When the shock wave is one quarter to one third of the way through the sample, 14 beams concurrently illuminate both sides of a 13 micron thick copper foil. These beams have a full width half maximum of 1 ns, and are focused down to 225 microns in diameter with energies from 200-250 Joules per beam. The plasma generated from this high energy laser predominantly emits He-α line radiation at 8.37 keV with a bandwidth of approximately 1%, with He-β line radiation at 9.86 keV at $\sim$10% of the intensity of the He-α line [14]. Here a 150 micron thick and 300 micron diameter tantalum pinhole is used to collimate the x-rays and also serves as a reference diffraction source, to enable accurate calibration of the location of the image plates relative to the sample and light source locations.

A schematic of the target used in these experiment and the diagnostic setup is shown in Figure 1 where more details of the x-ray diffraction diagnostic, PXRDIP, and experimental setup is described in the work by Rygg et al. [15]. The pressure in the sample is determined

by impedance matching the known Hugoniot of tantalum [16] and lithium fluoride (LiF)[17] using the measured velocity of the interface between the tantalum sample and the 100 micron thick (100)-oriented LiF window using the line-imaging VISAR diagnostic [18, 19].

The steadiness of the shock wave depends on the quality of the laser pulse shaping and in this campaign a few of the experiments had slightly increasing or decreasing interface velocities as a function of time due to random errors in the laser power. The implication of a non-steady wave in the context of a shock melt experiment is that the bulk of the sample may potentially see a slightly different shock pressure than what is inferred by impedance matching at the sample window interface. As it is the pressure the samples were shocked to that sets the entropy state in the sample, we must apply a systematic correction to the pressure determined by impedance match to account for the acceleration or deceleration of the wave as it transmits through the sample and interacts with the window, where impedance matching is performed. Following the work of Ali et al. [20], we were able to optimize a simulated interface velocity to the measured interface velocities, Figure 2, from which we can estimate how much acceleration or deceleration in the shock occurred and apply a correction to the impedance matching pressure. To ensure an accurate represeentation of the material response over the ranges considered in this experiment, we used analytical Mie-Gruneisen equation of state models for Tantalum and LiF fit to the Hugoniots of [**?**] and [17] within the ARES hydrocode. We found the deviation between the impedanced matched pressure and the average shock pressure observed by the sample could be different by up to 4% due to the slightly accelerating or decelerating nature of the shock in the tantalum, where it is the average shock pressure observed by the sample that is presented in Table 1. Any post-shock increase of decrease in pressure is adiabatic and should not be interpreted as the shock pressure required for melting.

The uncertainty in the shock pressure is then reported as a quadrature sum of the systematic error associated with impedance matching, which includes the LiF refractive index, LiF Hugoniot, tantalum Hugoniot, $\sim$2-4 GPa, the random uncertainty associated with the phase uncertainty in the VISAR diagnostic, 5% of the VPF, and then the random error associated with the correction from the impedance matched shock state to the average shock pressure observed in the sample. For this correction, we assume a conservative uncertainty estimate of 50% in the total correction, ranging from 0.5 to 5 GPa, which leads to a total uncertainty in the shock pressure of 4-5%.

III. RESULTS

Eight in-situ diffraction experiments were performed, ranging in tantalum shock states from 201 to 343 GPa. A summary of the experimental states achieved is shown in Table I. For shock pressures of 201±9 and 243±12 GPa, we observe only a single textured diffraction peaks from the shocked tantalum; the (110) BCC line. The (200) peak is not observed in these experiments. The expected ratio of intensities in the (110) to (200) peak is ∼5, if including the harmonic Debye-Waller factor, this expected ratio increases to 10. The peak intensity of the (110) line at a given ϕ angle has a signal to noise ratio of ∼60, however, because of texture, the minimum signal to noise ratio for the (110) peak falls to ∼ 6. Consequently, because of a combination of texture and the Debye-Waller effect, we do not see the (200) or other higher order diffraction lines.

A mixed-phase, partially molten state is first observed at a shock pressure of 264±16 GPa, where the diffuse scattering feature is observable at the same two-theta angle of the (110) peak of the solid component, the (110) peak has reduced in intensity by approximately a factor of two from the 243 GPa experiment and the diffuse scattering feature has a full width at half maximum 3.3 times greater than the solid component. The entrance of a broad diffuse scattering feature centered at the (110) peak of the bcc and the reduction of the intensity of the solid feature we take as evidence for the partial melting along the principal Hugoniot of tantalum. The same mixed phase diffraction signature is observed at shock pressures of 287±15 and 311±10. At shock pressures above 317±11 GPa, there is a loss of the solid diffraction signature and only the diffuse liquid scattering feature is observed. These transitions can be clearly observed in the raw data, as seen in the image plate panels shown in Figure 1. Lineouts of the dewarped x-ray diffraction data are shown in Figure 2, where the profiles are offset for clarity and the two lowest pressure solid phase lineouts are scaled by 0.5x to fit on the same intensity scale. One feature of the (110) diffraction line is that it does not increase in 2θ from shock pressures of 264 to 311 GPa. Based on hydrocode simulations optimized to the interface velocity measurements, the reason for this discrepancy is associated with the non-steadiness of the wave, where in the 264 GPa experiment the shock pressure rises behind the shock front to an average pressure of 276 GPa, increasing the density of the mixed phase system to an average density of 27.1 g cm^{-3} during the time of the x-ray exposure, in reasonable agreement with the measured 27.3±0.2

g cm^{-3}. The uncertainty in the density determined by diffraction is propagated from the uncertainty in the 2θ angle of the (110) peak. The uncertainty in the 2θ angle is taken as the quadrature sum of the misfits between the calibrated reference line positions and the known reference line, as well as the uncertainty in our determination of the (110) peak position.

In Figure 3, we present the diffraction data as a function of the shock pressure achieved in the sample and also the previous sound velocity measurements by [1] and [21] that are interpreted as signifying the melting transition. By comparing the slope changes in their measured sound velocities as a function of pressure and our transition pressures for incipient and complete melting, we can see that our transition pressures are within our pressure uncertainties; ∼10-20 GPa, of the transition pressures inferred from the sound velocity data. Furthermore, the diffraction data shows that if the first strong diffraction peak is interpreted as the (110) line of the BCC phase, then the densities are in excellent agreement with the measured tantalum Hugoniot densities.

To test if the measured diffraction data could also be consistent with the PNMA structure, we evaluated the density of the shocked tantalum assuming the first strong diffraction feature experimentally observed is the strongest line of the PNMA structures proposed in[9, 22]. As shown in Figure 3, the PNMA densities would not be consistent with the measured tantalum Hugoniot, where the uncertainty in the tantalum Hugoniot density is ∼1% and the PNMA phase density deviates by 4-6%. There are more recent suggestions by [23] of alternative energetically favorable phases, such as Cmcm, Fddd, and Pmma. As shown in Figure 4, these three structures share a strong diffraction peak with BCC at the same crystal density and hence cannot be immediately discarded due to density; however, they are also predicted to have strong diffraction lines at two-theta angles that are within the range observable of the PXRDIP and would not be expected to be sufficiently damped by the Debye-Waller effect. Consequently, we conclude that tantalum melts from the BCC phase.

IV. DISCUSSION

As in the work of [1], we do not measure temperature in these shock wave experiments, but we do accurately constrain the internal energy change from the ambient to the shocked state through the Rankine-Hugoniot equation. With some bounded assumptions for the electronic contribution to the heat capacity, [1] predicted the temperature for incipient melting

using available thermodynamic data, although they incorrectly interpreted the complete loss of shear strength as the incipient melting transition and not the complete melting transition. With the more recent shock temperature measurements of [2], we can directly constrain the electron thermal contribution as follows, with more details provided in the online supplemental material. The total internal energy change from the ambient to the shocked state is the sum of the change in energy along the cold curve, which we obtain from [24], as well as the change in thermal energy, which can be broken down into an ion thermal and electron thermal contribution. The ion thermal heat capacity can be accurately modeled with the Debye model and we parameterize the electron thermal model as was performed in [2]; however, we now use the [2] shock temperature measurements to fit the electron thermal contribution to the heat capacity. For calculating the Hugoniot across a phase transition, one must also account for the internal energy that goes into the latent heat at a given volume, $T\Delta S_m$, where we use entropy change of melting at constant volume of tantalum from [25] to determine ΔS_m. Shown in Figure 5 is our predicted Hugoniot along with uncertainties; which are based upon bounding the shock temperature data from [2] while forcing the incipient melting transition to occur at 254 GPa and completing at 315 GPa as determined from our diffraction data (marked along the Hugoniot).

At 254(15) GPa, we find a melt temperature of 8069(+1250,-750) K. The consistency between the ambient melt temperature and slope, the high pressure melt curve measurements of [3], and our inferred shock melt temperature suggests the dynamic and static high pressure communities are converging to the same answer. Adding confidence to the interpretation of our dynamic compression experiments is that the slope of the melt curve as predicted by the latent heat signature along the Hugoniot is in excellent agreement with the Simon fit, within 10% in slope.

Alternatively, if the discrepancy in the the static compression measurements of the tantalum melt curve, [4, 5], and the dynamic compression measurements shown here are interpreted to be solely due to kinetics, as discussed in [8, 9], the overdriving pressure for the melting transition would need to be >80 GPa. The level of agreement between these nanosecond x-ray diffraction results and the microsecond timescale x-ray diffraction experiments, ∼10 GPa, strongly suggests that superheating is insufficient to explain the level of disagreement between static and dynamic compression results, consistent with the conclusions of Luo et al. [12]. Furthermore, the observation of a two-phase region is also

inconsistent with the hypothesis that the melt curve is overdriven by 80 GPa in dynamic compression experiments, as the excess enthalpy in overdriving the transition by 80 GPa would be more than sufficient to completely melt the material as soon as the melt phase first nucleates, consequently one would never observe a mixed phase, which is inconsistent with our experimental observations.

V. CONCLUSIONS

Here we present in-situ x-ray diffraction measurements of tantalum shocked from $\sim$ 200 to 350 GPa. With increasing shock pressure, we observe the transition from BCC tantalum, to a mixed phase of BCC and liquid at 254$\pm$15 GPa, to completely liquid tantalum at 317$\pm$10 GPa. Proposed alternative structures of tantalum are not observed at the high temperatures and pressures in this work, providing confidence that BCC is the stable high temperature phase. The transition pressures observed in these nanosecond timescale experiments are compared to the incipient and complete melting transition pressures observed in microsecond timescale gas gun experiments, and we find them to be in excellent agreement. The degree of experimental agreement between these significantly disparate timescale experiments and the observation of a mixed phase itself suggests that kinetics of melting is insufficient to explain the discrepeacy in some static and dynamic compression experiments for measuring the melting curve of tantalum. With our accurate characterization of the melting transition pressures along the Hugoniot, we are able to use the shock temperatures of Dai et al. [2] to infer a high pressure melting temperature and slope that are consistent with both ambient data and recent static high pressure data by Dewaele et al. [3], which provides confidence that we are converging on the true high pressure melt curve of tantalum.

ACKNOWLEDGMENTS

We acknowledge the target fabrication efforts of C. Davis and support at the Laboratory for Laser Energetics by C. Sorce, N. Whiting, and J. Tellinghuisen. This work was performed under the auspices of the U.S. Department of Energy by Lawrence Livermore National

Laboratory under Contract DE-AC52-07NA27344.

---

[1] J. Brown, J. Shaner, Rarefaction velocities in shocked tantalum and the high-pressure melting point, in: Proceedings of the American Physical Society Shock Compression of Condensed Matter, 1983, doi:10.2172/5962493.

[2] C. Dai, J. Hu, H. Tan, Hugoniot temperatures and melting of tantalum under shock compression determined by optical pyrometry, Journal of Applied Physics 106 (2009) 043519, doi:10.1063/1.3204941.

[3] A. Dewaele, M. Mezouar, N. Guignot, P. Loubeyre, High melting points of tantalum in a laser-heated diamond anvil cell, Phys. Rev. Lett. 104 (2010) 255701, doi:10.1103/PhysRevLett.104.255701.

[4] D. Errandonea, B. Schwager, R. Ditz, C. Gessmann, R. Boehler, M. Ross, Systematics of transition-metal melting, Phys. Rev. B 63 (2001) 132104. doi:10.1103/PhysRevB.63.132104.

[5] D. Errandonea, M. Somayazula, D. Hausermann, H. K. Mao, Melting of tantalum at high pressure determined by angle dispersive x-ray diffraction in a double-sided laser heated diamond-anvil cell, Journal of Physics: Condensed Matter 15 (45) (2003) 7635–7649, doi:10.1088/0953-8984/15/45/003.

[6] A. Karandikar, R. Boehler, Flash melting of tantalum in a diamond anvil cell to 85 GPa, Phys. Rev. B. 93 (2016) 054107, doi:10.1103/PhysRevB.93.054107.

[7] L. Vocadlo, D. Alfe, G. D. Price, M. J. Gillan, First principles calculations on the diffusivity and viscosity of liquid Fe-S at experimentally accessible conditions, Physics of the Earth and Planetary Interiors 120 (2000) 145–152.

[8] D. Errandonea, Improving the understanding of the melting behaviour of Mo, Ta, and W at extreme pressures, Physica B: Condensed Matter 357 (3) (2005) 356 – 364, doi:10.1016/j.physb.2004.11.087.

[9] C. M. Liu, C. Xu, Y. Cheng, X. R. Chen, L. C. Cai, Melting curves and structural properties of tantalum from the modified-z method, Journal of Applied Physics 118 (23) (2015) 235901. doi:10.1063/1.4937563.

[10] R. Hrubiak, Y. Meng, G. Shen, Microstrucgtures define melting of molybdenum at high pressures, Nature Communications 8 (14562), doi:10.1038/ncomms14562.

[11] S. N. Luo, T. J. Ahrens, T. Cagin, A. Strachan, W. A. Goddard, D. C. Swift, Maximum superheating and undercooling: Systematics, molecular dynamics simulations, and dynamic experiments, Physical Review B 68 (2003) 134206, doi:10.1103/PhysRevB.68.134206.

[12] S. N. Luo, T. J. Ahrens, Shock-induced superheating and melting curves of geophysically important minerals, Physics of the Earth and Planetary Interiors 143-144 (2004) 369–386, doi:10.1016/j.pepi.2003.04.001.

[13] J. Wang, F. Coppari, R. Smith, J. Eggert, A. Lazicki, D. Fratanduono, J. Rygg, T. Boehly, G. Collins, T. Duffy, X-ray diffraction of molybdenum under shock compression to 450 gpa, Physical Review B 92 (2015) 174114. doi:10.1103/PhysRevB.92.174114.

[14] F. Coppari, R. F. Smith, D. B. Thorn, J. R. Rygg, D. A. Liedahl, R. G. Kraus, A. Lazicki, M. Millot, J. H. Eggert, Optimized x-ray sources for x-ray diffraction measurements at the omega laser facility, Review of Scientific Instruments 90 (12) (2019) 125113. doi:10.1063/1.5111878.

[15] J. R. Rygg, J. H. Eggert, A. E. Lazicki, F. Coppari, J. A. Hawreliak, D. G. Hicks, R. F. Smith, C. M. Sorce, T. M. Uphaus, B. Yaakobi, G. W. Collins, Powder diffraction from solids in the terapascal regime, Review of Scientific Instruments 83 (2012) 113904, doi:10.1063/1.4766464.

[16] A. Mitchell, W. J. Nellis, Shock compression of aluminum, copper, and tantalum, J. Appl. Phys. 52 (1981) 3363. doi:10.1063/1.329160.

[17] P. A. Rigg, M. D. Knudson, R. J. Scharff, R. S. Hixson, Determining the refractive index of shocked [100] lithium fluoride to the limit of transmissibility, Journal of Applied Physics 116 (2014) 033515, doi:10.1063/1.4890714.

[18] L. M. Barker, R. E. Hollenbach, Shock-wave studies of pmma, fused silica, and sapphire, J. Appl. Phys. 41 (1970) 4208–4226.

[19] P. M. Celliers, G. W. Collins, L. B. Da Silva, D. M. Gold, R. Cauble, Accurate measurement of laser-driven shock trajectories with velocity interferometry, Applied Physics Letters 73 (10) (1998) 1320–1322, doi:10.1063/1.121882.

[20] S. J. Ali, R. G. Kraus, D. E. Fratanduono, D. C. Swift, J. H. Eggert, An iterative forward analysis technique to determine the equation of state of dynamically compressed materials, J. Appl. Phys. 121 (2017) 195901, DOI:10.1063/1.4983067.

[21] M. Akin, J. Nguyen, M. Beckwith, R. Chau, W. Ambrose, O. Fat'yanov, P. Asimow, N. Holmes, Tantalum sound velocity under shock compression, Journal of Applied Physics

125 (14) (2019) 145903, doi:10.1063/1.5054332.

[22] Y. Yao, D. D. Klug, Stable structures of tantalum at high temperature and high pressure, Phys. Rev. B 88 (2013) 054102, DOI:10.1103/PhysRevB.88.054102.

[23] J. B. Haskins, J. Moriarty, Polymorphism and melt in high-pressure tantalum. II. Orthorhombic phases, Phys. Rev. B 98 (2018) 144107, doi:10.1103/PhysRevB.98.144107.

[24] A. Dewaele, P. Loubeyre, M. Mezouar, Equations of state of six metals above 94 GPa, Phys. Rev. B. 70 (2004) 094112.

[25] D. C. Wallace, Statistical Physics of Crystals and Liquids, World Scientific, Singapore, 2002.

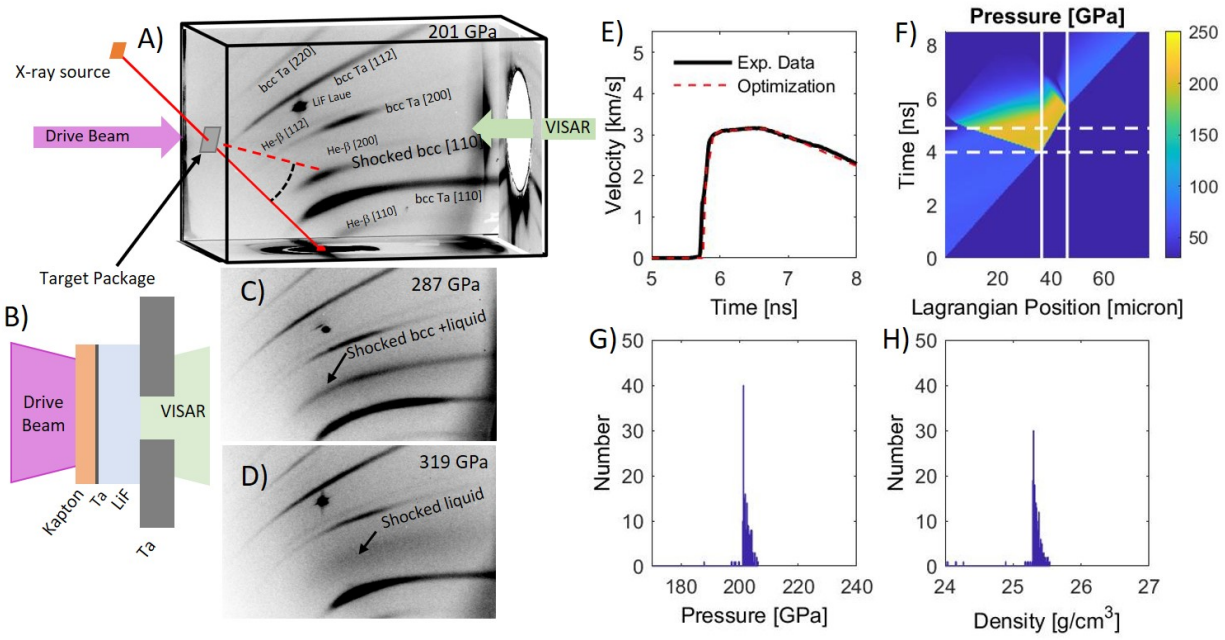

FIG. 1. Schematic of the target, A), diagnostic, B), including raw data from three experiments at pressures of 201±9, 287±15, and 319±15, B-D). At the downrange side of the PXRDIP diagnostic box, a 50 mm hole is located on the PXRDIP box to allow for the line-VISAR diagnostic to measure the interface velocity at the tantalum-LiF interface. The VISAR data is used for direct impedance matching to determine the pressure of the shock in the tantalum, but also as input for a forward optimization, E), from which one can infer the pressure history in the sample, F), a pressure histogram at the time of x-ray exposure G), and the expected density histogram H).

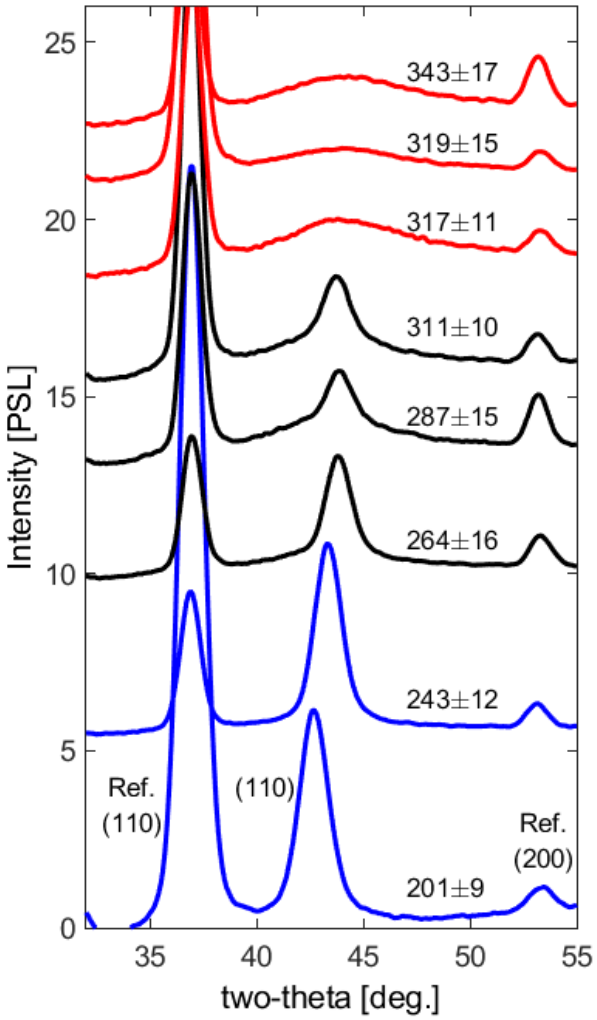

FIG. 2. Lineouts from the image plates are offset for clarity and colored according to the phase assemblage observed; blue for solid only, black for solid and liquid, and red for liquid only. Beyond the offset, the solid only lineouts shown in blue are reduced in magnitude by a factor of two. Also included are the hkl indices of the shocked data and the reference pinhole lines as well as the associated pressures in GPa for each lineout and estimated uncertainty.

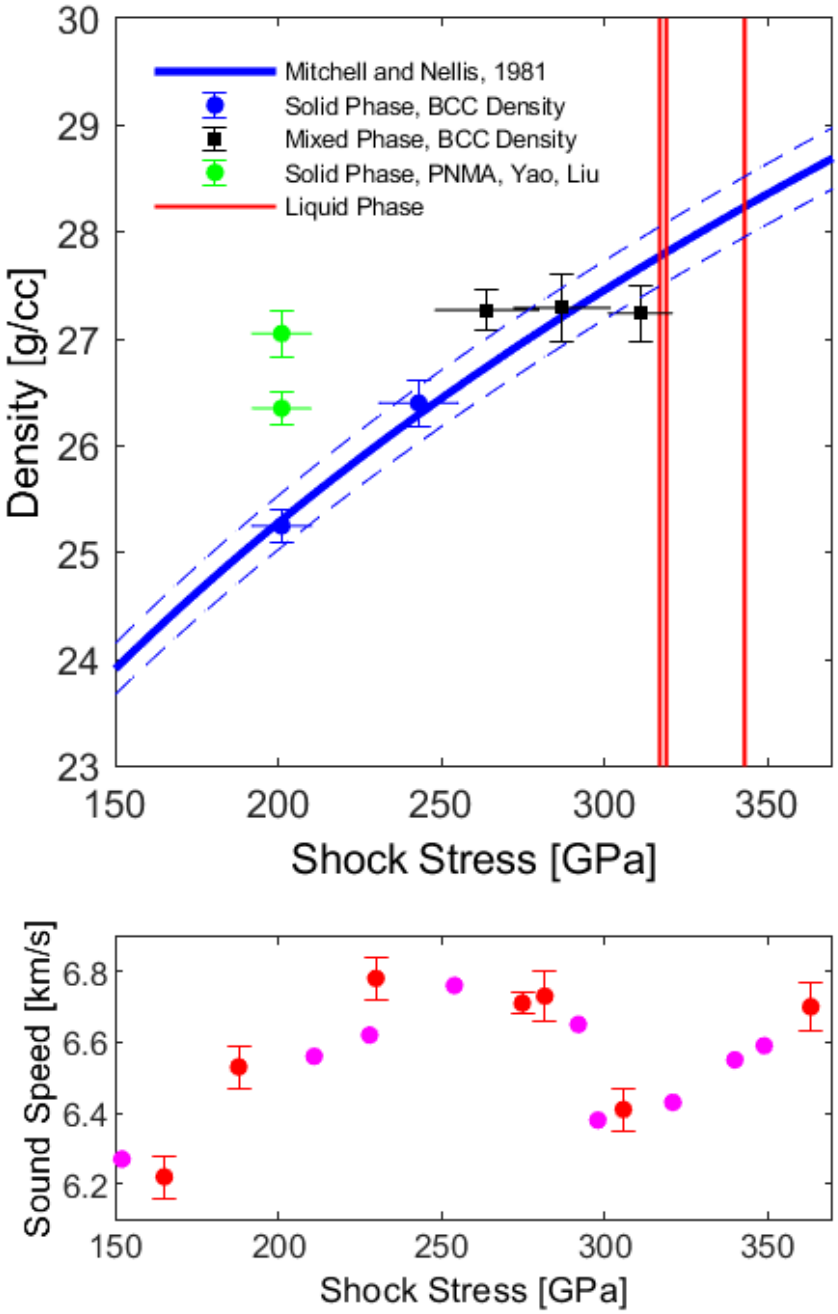

FIG. 3. Top: Measured density of the solid phase observed in each diffraction experiment assuming the phase is BCC. The tantalum Hugoniot[16] is shown in the solid blue line with uncertainties bounds as dashed blue lines. Shown in green is the interpretation of the diffraction data if the first strong diffraction peak is inferred to be due to the PNMA phase [9, 22]. The pressures at which liquid diffraction data are observed are shown with the red vertical lines. Bottom: Sound velocity data of tantalum from Brown and Shaner [1], magenta, and [21], red, with the same pressure axis as above.

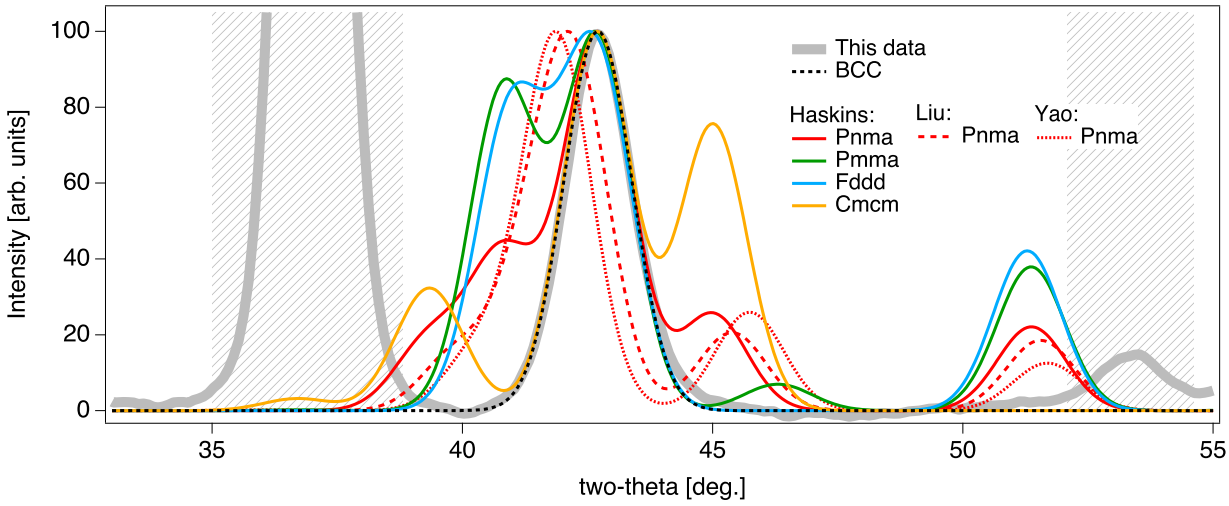

FIG. 4. Comparison of experimental diffraction data with recently proposed structures for the high temperature phases of tantalum by [9, 22, 23] where the diffraction patterns are calculated with the approximate instrumental resolution of the PXRDIP diagnostic,$\sim$1.6 degrees, at the density on the Hugoniot of tantalum at 200 GPa, 25.25 g cm^{-3} and photon wavelength of 1.483 angstroms. Hatched vertical bands represent regions where the reference pinhole lines dominate the diffraction pattern.

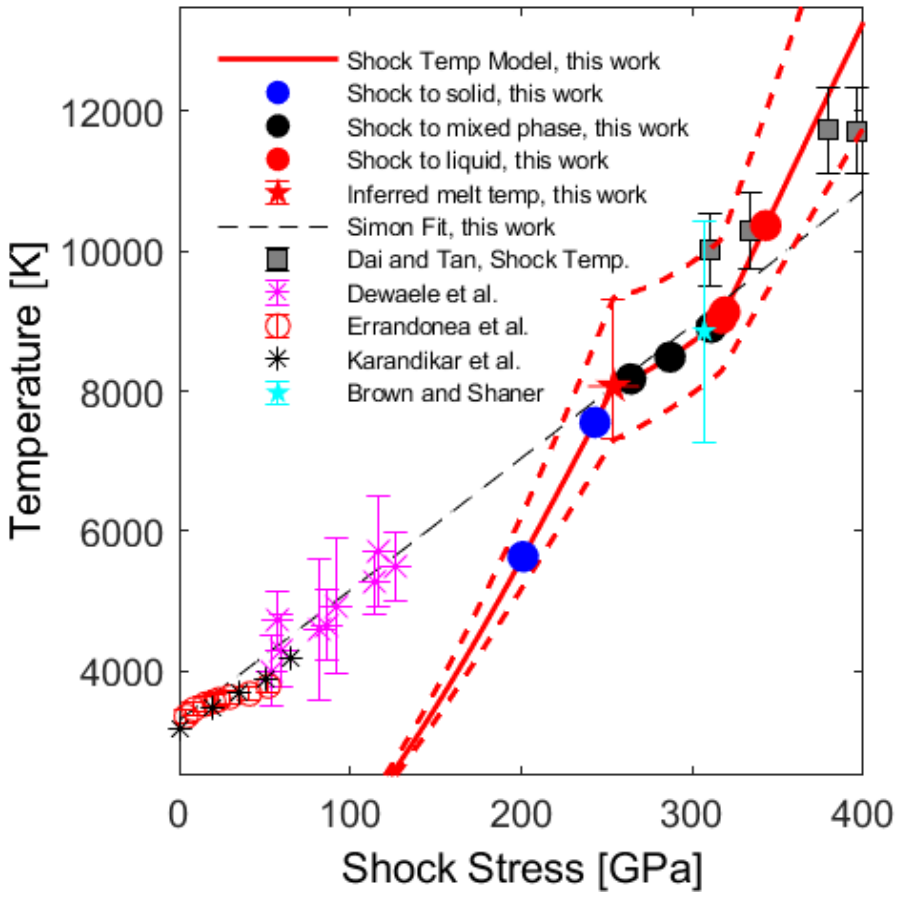

FIG. 5. The temperature along the Huogniot and its uncertainty, red solid and dashed lines, is constrained by the shock temperature measurements by [2], gray squares, with more details provided in the online supplemental material. The phases observed at a given pressure along the Hugoniot, solid, mixed, and liquid, are plotted at the calculated temperature, using large filled blue, black, and red circles, respectively. From the calculated shock temperatures, we infer a high pressure melting temperature at the pressure for incipient melting determined here, red star. This high pressure melt datum and ambient temperature melt datum is fit to the Simon melt equation, $T=3293(P/185.5+1)^{1.04}$, black dashed line, which is compared to the static melt curve measurements of [3–6]. Also compared is the previous dynamic compression sound speed measurement of [1], where temperature is calculated using a similar thermodynamic model but without the constraints of temperature data from [2].

TABLE I. Summary of the data observed in each experiment

Experiment No.	Interface Velocity [km s^{-1}]	Shock Pressure [GPa]	Phase	Solid Phase Density [g cm^{-3}]
75280	3.10 ± 0.08	201 ± 9	BCC	25.25 ± 0.15
75293	3.54 ± 0.08	243 ± 12	BCC	26.40 ± 0.22
75284	3.75 ± 0.12	264 ± 16	BCC+Liquid	27.27 ± 0.19
75295	3.90 ± 0.12	287 ± 15	BCC+Liquid	27.29 ± 0.31
75282	4.05 ± 0.07	311 ± 10	BCC+Liquid	27.24 ± 0.26
75289	4.15 ± 0.08	317 ± 11	Liquid	NA
75291	4.22 ± 0.10	319 ± 15	Liquid	NA
75287	4.43 ± 0.09	343 ± 17	Liquid	NA